

A vision transformer-based framework for knowledge transfer from multi-modal to mono-modal lymphoma subtyping models

Bilel Guetarni¹, Feryal Windal², Halim Benhabiles², Marianne Petit³, Romain Dubois³,
Emmanuelle Leteurtre³, and Dominique Collard⁴

¹Centrale Lille, UMR 8520, Lille, France

²Junia, UMR 8520, CNRS, Centrale Lille, University of Polytechnique Hauts-de-France, Lille,
France

³Department of Pathology, University Hospital of Lille, Lille, France

⁴LIMMS/CNRS-IIS The University of Tokyo, IRL 2820, Lille, France

Abstract

Determining lymphoma subtypes is a crucial step for better patients treatment targeting to potentially increase their survival chances. In this context, the existing gold standard diagnosis method, which is based on gene expression technology, is highly expensive and time-consuming making difficult its accessibility. Although alternative diagnosis methods based on IHC (immunohistochemistry) technologies exist (recommended by the WHO), they still suffer from similar limitations and are less accurate. WSI (Whole Slide Image) analysis by deep learning models showed promising new directions for cancer diagnosis that would be cheaper and faster than existing alternative methods. In this work, we propose a vision transformer-based framework for distinguishing DLBCL (Diffuse Large B-Cell Lymphoma) cancer subtypes from high-resolution WSIs. To this end, we propose a multi-modal architecture to train a classifier model from various WSI modalities. We then exploit this model through a knowledge distillation mechanism for efficiently driving the learning of a mono-modal classifier. Our experimental study conducted on a dataset of 157 patients shows the promising performance of our mono-modal classification model, outperforming six recent methods from the state-of-the-art dedicated for cancer classification. Moreover, the power-law curve, estimated on our experimental data, shows that our classification model requires a reasonable number of additional patients for its training to potentially reach identical diagnosis accuracy as IHC

technologies.

1 Introduction

Diffuse Large B-Cell Lymphoma (DLBCL) is the most common type of non-Hodgkin lymphoma (NHL), accounting for 30% to 40% of NHL cases [1, 2, 3]. DLBCL has a significant worldwide impact, with an estimated 544,352 new cases and 259,793 deaths in 2020 [4]. For instance, the number of new cases and deaths is expected to increase globally in the next years, with a projected number of DLBCL cases increase of 7% in Western Europe from 2020 to 2025 [5]. The works of [6], have permitted to demonstrate that DLBCL can be categorized into two molecular subtypes namely the ABC (activated B-cell-like) and GCB (germinal-center B-cell-like). Moreover, it has been shown that identifying the subtype is crucial for treatment selection and vital prognosis of the patient [6, 7, 8, 9]. Specifically, patients with the ABC subtype have a survival rate of 30% over 5 years while those with the GCB have 75% [2, 7]. Nevertheless, the recent clinical trials using new targeted treatments have shown promising results in term of efficiency and survival chance improvement, notably for the patients with the most aggressive subtype (ABC) [10, 11].

Currently, the gold standard for DLBCL subtyping is RT-MLPA (*reverse transcriptase multiplex ligation-dependent probe amplification*) which is a molecular

biology method [7]. However, this method is expensive and time-consuming. Indeed, the cost estimated for one patient is 600€ and the time response estimated for the diagnosis is 35 days (information provided by pathologists of the Lille University Hospital). Therefore, there is a need to develop alternative methods that are more cost-effective and time efficient than RT-MLPA.

In this context, previous subtyping methods based on microscopic examination of the patient tissue by the pathologist are still exploited in addition to the gold standard. More specifically this visual examination is performed on tissue stained with mainly two types of markers, namely IHC¹ (immunohistochemistry) and HES (hematoxylin-eosin-safran) markers. In the case of IHC, the expression levels of three proteins are quantified by the pathologist which permits to determine the DLBCL subtype based on the Hans algorithm [3]. Although the response time of this later method is relatively fast and its cost is reasonable compared to the gold standard, it has an error rate of 20% (misclassified cases with respect to the gold standard) and requires the involvement of the pathologist for the tissue examination which represents a fastidious task, notably in daily routines. In the case of HES, which is the combination of three histologic stains, the pathologists analyze the morphology and structural organization of the tissue cells. However, due to the high similarity of these features between the two subtypes and the lack of objective criteria, the pathologists struggle to reach an agreement in their decision which is affected by their subjective perception. Compared to the IHC, the HES analysis is less expensive (doesn't requires protein markers) but suffers from a higher error rate with respect to the gold standard.

With the rapid increase of data in medical centers, there have been a growing interest to apply deep learning methods to medical image analysis [12, 13, 14]. In the field of histopathology, slides of tissue samples can be digitized into high-resolution images named Whole Slide Images (WSI). Deep learning methods have shown unprecedented performance on many automatic tasks on these images [15]: detection of several cancers (e.g. breast, lung, colon, etc. [16, 17, 18]), nuclei segmentation [19] or case/image similarity [20, 21, 22]. Yet, automatic differentiation of DLBCL subtypes based on WSI has received few attention in the literature. Among the main reasons that could explain this observation is the scarcity of publicly available annotated datasets (data protection and privacy). In addition, the characterization of the two subtypes of DLBCL from WSI is a challenging task. Indeed, the diversity of the cancer

location in the patient's body and the complex nature of the tissue, results into a high intra-class variability for each subtype. Besides, the extremely high resolution of WSI prevents the direct application of neural networks and involves high demanding computational requirements.

In this work, we propose a deep learning based framework for distinguishing between the ABC and GCB subtypes of DLBCL cancer from high-resolution Whole Slide Images (WSI). Our framework involves the development of a multi-modal deep architecture, serving as a teacher model for classifying the cancer subtypes using various WSI modalities, namely IHC-BCL6, IHC-CD10, IHC-MUM1 and HES. Additionally, we leverage the concept of knowledge distillation to build a mono-modal classifier, referred to as the student model, which shows promising performance for differentiating between the subtypes using a single modality, namely HES. It is worth mentioning that having a subtyping method based only on HES modality is of high interest for the health care system (pathologists, patients, laboratories). Indeed, removing the three IHC modalities will permit to (i) lighten the data acquisition process in the laboratories, (ii) accelerate the patient diagnosis and (iii) avoid the costs related to the production of these modalities.

The main contributions of this work are the following:

- We exploit the concept of knowledge distillation for efficiently driving the learning of a classifier following a *4-to-1 WSI modality* training process. In this sense, the teacher model is used to support the student one to extract the most relevant features for DLBCL subtypes characterization. In addition, we propose a generic design of the framework enabling its application for any classification task that requires knowledge transfer from a multiple inputs classifier to a unique input classifier.
- We designed and developed a deep architecture tailored for handling multi-modal inputs (4 modalities of WSI) in a one-shot pass. To deal with the extremely high-resolution (100,000 × 100,000 px on average which represent several billion pixels) of these inputs, we incorporated in our architecture a ViT encoder which permits to process them in the form of a sequence of patches.
- We designed and developed a module offering a cross-stain attention mechanism that is applied on the ViT encoder outputs (one per modality), to learn the optimal weighted aggregation of IHC and HES features.
- We conducted a comprehensive experimental study

¹Alternative diagnosis method recommended by the WHO when RT-MLPA is not available.

to demonstrate the efficiency of our method and its superiority compared to the state-of-the-art approaches.

2 Related works

Recently, Guidolin et al. [23] have proposed an experimental study on 30 DLBCL patients (15 ABC vs 15 GCB) that aims to quantify, using statistical measures, their cells spatial distribution from WSIs (stained with five IHC protein markers). As raised by the authors, their experimental study has permitted to highlight that the combination of spatial statistics-derived parameters can be exploited for distinguishing between ABC and GCB. However, no automatic subtyping method has been further proposed.

Despite the limited research works on automatic methods for DLBCL subtyping, there is a vast literature on cancer classification from WSI, notably using deep neural networks [15, 24, 25, 16, 18, 26, 27, 28]. Among these works, several ones have addressed the differentiation between DLBCL and other lymphoma types [29, 30, 31, 32, 33, 34]. For example, Hashimoto et al. [33] proposed a CNN-based classification method to distinguish between three lymphoma cancers, namely DLBCL, AITL and CHL, from HE WSIs. To deal with the high resolution of WSIs they made the choice to subdivide them into a set of patches and adopted a Multiple Instance Learning (MIL) approach to train the final classifier. To improve the performance of the classifier they proposed a methodology which permits to select, during the training stage, the most relevant WSIs of the dataset. More specifically, they defined a typicality criterion that permits to measure the relevance of each WSI in term of cancer class representativeness.

In addition to the task of cancer classification from WSI, other works proposed a higher level of cancer analysis related application, namely patient survival prediction [35, 27]. In the case of [35], the authors designed a multi-modal graph neural network architecture to train a model to predict survival chances in cases of bladder and ovarian cancer from WSI IHC modalities. As raised by the authors, utilizing a GNN enables to extract cell-centric features and process the WSI in a single forward pass. In the case of Chen et al.[27], they proposed a backbone composed of a series of vision transformers units to encode multi-scale region features. To this end, they choose to feed these units by exploiting the levels of a pyramidal representation of the WSI where each level corresponds to a subdivision into patches of customized size. To improve the performance of their model they pretrained it by adopting a self-supervised learning strategy.

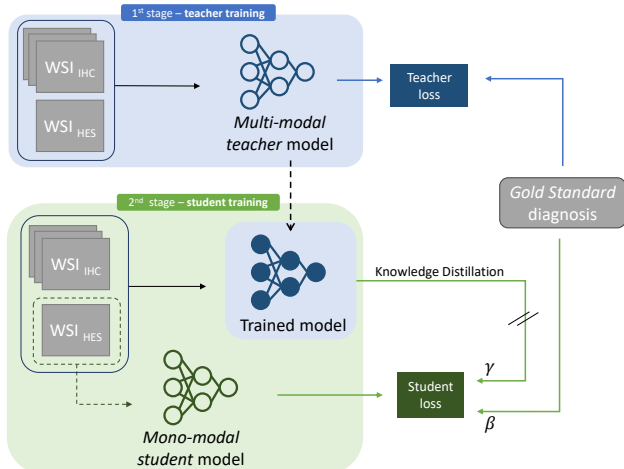


Figure 1: Knowledge Distillation for multi-to-mono modal WSI subtyping model.

Other works have been proposed to address others disease diagnosis from WSIs such as colorectal polyps classification [36], neurodegenerative disease diagnosis [37] or virus infected cells identification [38]. For instance, the method proposed by Dwivedi et al. [39] performs liver disease severity scoring from two WSIs modalities, namely Masson’s trichrome and HES. For each modality, a CNN generates a heatmap of the WSI which is subsequently transformed into a graph representation. Each heatmap is then processed by a graph neural network (GNN) to produce a vector that captures the characteristics of the WSI. The disease severity score is predicted from the concatenation of the two modality vectors.

It is worth mentioning that previously to our work, Hu et al. [40] have proposed a brain tumor segmentation method that exploits the concept of knowledge distillation for addressing the multi-to-mono modal learning issue. Although our work is based on a similar approach, our method is completely different since it has been tailored to perform a different task (tissue classification instead of tumor segmentation) on data of different nature and characteristics (high resolution microscopic images instead of low-resolution MR scans).

3 Methods

As illustrated in Fig 1, our framework designed for cancer subtyping from WSIs includes two classification models which are built by following a two-stage training process. In the first stage, a multi-modal teacher classifier is trained on HES and IHC modalities. In the second stage, the teacher acts through a knowl-

edge distillation process as a robust supervision source for training a mono-modal student classifier on HES modality.

Our deep learning architecture is summarized in Fig. 3 and we next detail each component.

3.1 From multi-slides input to single prediction

In what follows, we describe the process by which our methodology exploit the HES and IHC WSIs.

To avoid excessively complex computations related to the size of the regions, we adopted a region-based sampling approach. It involves extracting matching regions of interest between all WSI modalities (see Fig. 2). For each region R and each modality m , we defined a grid composed of RGB patches $x \in \mathbb{R}^{p \times p \times 3}$, with size $p \times p$, and we constructed sequences X of these patches.

Let N denotes the number of patches in this grid and S represent the number of patches in a sequence, such that $X \in \mathbb{R}^{S \times p \times p \times 3}$. The sequence extraction process consists in sampling a uniformly distributed sequence of S patches from the grid, without replacement. This process is repeated until $N < S$ (i.e. there are less than S patches left in the grid). Let's R_m be the set of all sequences extracted from region R of modality m . We randomly associate one sequence per modality to form a bag B , that is:

$$B := \{X_m, \forall m \in M\} \quad (1)$$

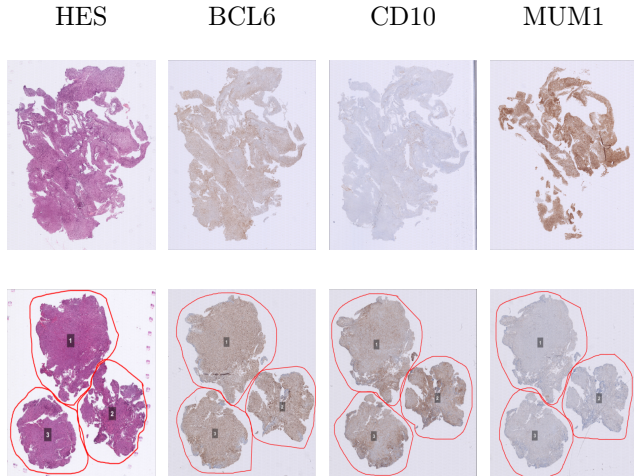


Figure 2: Examples of HES and IHC WSIs. **First row** shows an example for which the MUM1 modality is visually very different from the other ones; while in the **second row** all modalities are similar. The regions are annotated (in red) and an id number is assigned to allow cross-stain region matching.

where $X_m \in R_m$ and M is the set of modalities. Note that the sequences are sampled without replacement from each modalities. Indeed, when all sequences of one modality have been used, no more bags can be formed. These bags are the input to the multi-modal model (i.e. teacher model).

Given that regions are represented as series of patches, we utilize the ViT architecture [41] as our feature extractor. Furthermore, this architecture has the capacity to learn inter-element relationships via its self-attention mechanism, which is of high interest in the case of WSI patches [27, 26]. The ability to understand and leverage these relationships is crucial to learn global representation of WSIs.

To classify an image, the ViT architecture [41] transforms the image into a sequence of patches. These patches are subsequently flattened and projected by a linear layer into vectors known as patch embeddings. In addition to this sequence, a learnable class token is prepended, serving as the image embedding post-encoder for the purpose of classification. Our approach adheres to a similar structure; we flatten the patches of the sequences, project them with a linear layer, and prepend a class token. However, in our scenario, we are working with a bag of sequences representing the same object but manifesting across different modalities (i.e., stains). To account for variations in color distribution among these modalities, we employ a separate projection layer for each one. The learnable class token embedding, however, is shared across all modalities. The bag sequences are independently encoded by a shared ViT encoder and subsequently normalized with a Global Layer Normalization (GLN) [42]. All sequences X_m of the bag B are encoded and normalized simultaneously:

$$Z_m = GLN(Encoder(X_m)) \quad (2)$$

where *Encoder* is the ViT encoder (including patch flattening and linear projection) and *GLN* is the Global Layer Normalization. We use the class token embeddings from every sequence after this GLN as input to our cross-stain attention mechanism which produces the bag representation. In our experimental study, we found that adding a softmax activation after the encoder's MLP improves validation results. In what follows we refer to this modified version of the encoder unless otherwise stated.

3.2 Cross-stain attention

We design our cross-stain attention mechanism (Fig. 4) to infuse information from IHC into HES embeddings. For this, we consider HES as a query that is used to

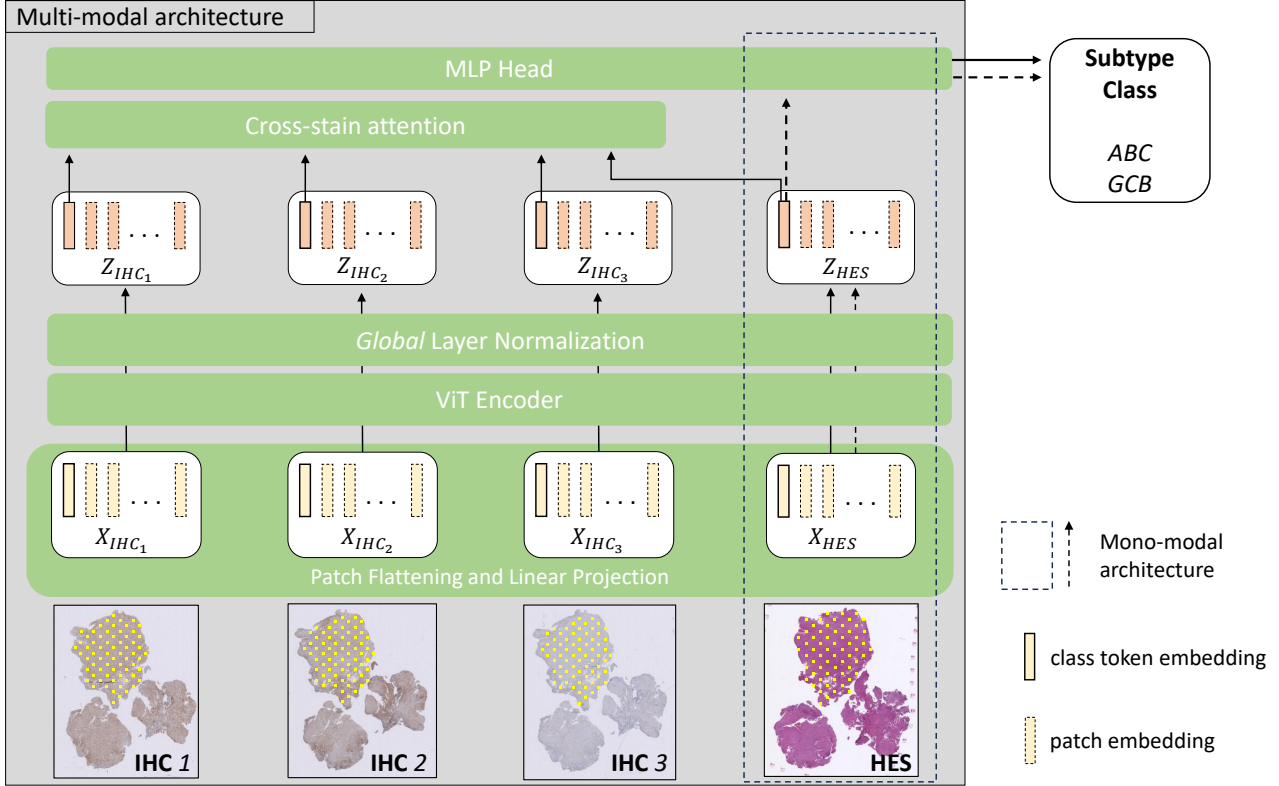


Figure 3: Our multi-modal architecture (teacher) takes as input a bag of sequences uniformly sampled from the same region across all WSI modalities (yellow squares). Its cross-stain attention mechanism learns to fuse HES and IHC information to produce a bag representation for multi-modal WSIs classification. Our mono-modal architecture is presented within the dotted bounding-box on the right.

pull information from IHC embeddings. Whereas the current popular attention mechanism is defined as the

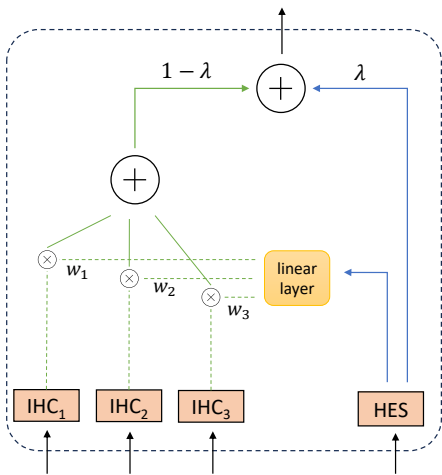


Figure 4: Cross-stain attention mechanism which fuses HES and IHC information.

dot-product attention between a query and keys [41], in our case different modalities are involved; making the dot-product based attention unsuitable. When the query and keys come from different space regions, it becomes less relevant to base attention on the dot-product similarity between the representation of the query and keys. In our case, this is particularly evident as HES images exhibit a significantly different color distribution than IHC images (see Fig. 2). In this regard, we define a tailored attention mechanism where the attention weights are not calculated as a dot-product between the query and the keys, but are predicted by a linear layer from the query.

Let's z_{HES}^0 be the HES class token embedding (initialized with the shared learnable class token) following the GLN. Similarly, let's $z_{IHC_i}^0$ be the class token embedding from IHC i . The cross-stain attention starts by predicting IHC attention weights with a linear layer from the HES class token embedding:

$$w = Wz_{HES}^0 \quad (3)$$

This linear layer outputs a k -dimensional vector, with

k the number of IHC stains ($k = 3$ in our case). We then perform a weighted sum of the IHC class token embeddings using these weights and add it to the HES one:

$$z_B = \lambda z_{HES}^0 + (1 - \lambda) \sum_{i=1}^k w_i z_{IHC_i}^0 \quad (4)$$

where λ is a trade-off coefficient between HES and IHC information. The output of our attention mechanism is a vector representation of the bag B . This vector is then fed to a classification head for subtype classification.

In the first stage, the multi-modal model is trained to minimize the cross-entropy loss with the ground-truth of the WSI from which the bag is sampled.

3.3 Knowledge Distillation from multi to mono modality WSI classification

We utilize KD to transform the multi-modal model, initially trained including both IHC and HES data (teacher), into a mono-modal one that is solely reliant on HES data (student). During the training of the student, we feed to the teacher the bag of sequences, while the student predicts the subtype from the HES sequence only. Because the student doesn't make use of IHC we remove the cross-stain attention mechanism; indeed, the HES class token (z_{HES}^0) after the LN is then directly fed to the classification head. After the teacher model has finished training, it produces outputs that are the corresponding probability predictions for each class. Subsequently, the student model begins its training stage. The student model's progress is supported by leveraging the outputs from the teacher model in addition to the ground-truth. The objective during the training phase of the student model is to minimize the cross-entropy between its own predictions and those of the teacher model, as well as between its predictions and the actual target. In this study, we implement knowledge distillation in the form of hard distillation, indicating that we treat the teacher model's prediction as a hard target for the student model's training. If f^t and f^s denote the teacher and student models respectively, X^t and X^s their corresponding inputs, and y the ground-truth, the student model loss function is defined as:

$$Loss = \beta \mathcal{L}(y, f_s(X^s)) + \gamma \mathcal{L}(f_t(X^t), f_s(X^s)) \quad (5)$$

where \mathcal{L} is the cross-entropy loss function, β and γ are the ground-truth and teacher supervision coefficients respectively. We convert the teacher's output to hard labels and apply label smoothing [43] with a parameter of $\alpha = 0.1$ to both the teacher's prediction and the true label.

4 Experiments

4.1 Data description and processing

We dispose of a collection of WSIs from patients of the Lille University Hospital diagnosed with DLBCL between 2010 and 2020. The collection has been meticulously inspected by a pair of pathologists, senior and junior. The patients subtyping was carried out in three distinct manners:

- pathologist diagnosis based on visual examination of the HES WSI
- application of the Hans algorithm [3]
- execution of RT-MLPA [2]

However, given that RT-MLPA is recognized as the gold standard for DLBCL subtyping, we take its result as the ground-truth for the subtyping of patients.

Our dataset is made up of 204 patients, of which 94 are diagnosed with the ABC subtype, 66 with GCB, and 44 do not fall into either category (being either *unclassifiable* or *primary mediastinal large B-cell lymphoma*). We have excluded these 44 patients from our dataset. Additionally, we removed 3 patients due to the absence of cancerous tissue in their HES WSI. For the training phase, we selected 93 patients out of the remaining 157 subjects. For these patients, we were able to successfully match the HES WSI with their corresponding IHC WSIs (BCL6, CD10, and MUM1). During the first stage, the teacher is trained with the entire bag of sequences containing all modalities, while in the second stage (KD), the student is trained with the HES sequences only. As seen in Fig. 2, only the patients with a perfect match across all four markers were selected for the training phase. For the testing phase, we include the remaining portion of the dataset, which consists of 64 patients with a single HES WSI. The train set patients are randomly separated into training and validation according to a 80:20 split.

All slides were scanned with a Ventana iScan HT at $\times 40$ magnification ($0.25 \mu m$ per pixel). For data pre-processing, the tissue was separated from the background through gaussian blurring and Otsu thresholding segmentation. Then, we extracted sequences of patches with $S = 256$ and $p = 32$ at $\times 20$ magnification (each patch is $16 \times 16 \mu m$). Our dataset covers 38 different tissue types such as: lymph node (42%), brain (13%), mediastinum (5%), soft tissue (5%), bone (4%), etc. This large diversity of tissue location results in very heterogeneous image characteristics among DLBCL images.

Table 1 provides a summary of the distribution of sequences by modality and the distribution of patients in the training and testing splits.

Table 1: Data summary: number of patients for each set. Training patients were split into 80:20 for train and validation.

	train		test		total
	ABC	GCB	ABC	GCB	
sequences					
<i>BCL6</i>	83K	33K			116K
<i>CD10</i>	82K	33K			115K
<i>MUM1</i>	80K	35K			115K
<i>HES</i>	78K	35K	34K	32K	179K
patients	59	34	33	31	157

4.2 Experimental settings

For both teacher and student models we use a ViT encoder ($d=128$, $n=3$, $h=2$), with a 2-layer MLP (a 384-dimensional hidden layer and a softmax activation after the second layer). The classification head is a trainable linear layer with two output neurons (one for each subtype) and a softmax activation to transform its output to a probability distribution over the subtypes. To determine a patient subtype, we apply major voting on all the sequences prediction coming from this patient. The teacher is trained with a batch of 32, where each sample of the batch is a bag of sequences (B). We use an initial learning rate of 8.10^{-5} with a learning rate decay of 0.5 every 5 epochs. The student is trained with a batch of 64 and a constant learning rate of 10^{-5} . For both models, we adopt the Adam optimizer with clipping gradient (max norm of 3 for teacher and 5 for students) and apply label smoothing ($\alpha = 0.1$) to the ground-truth. The models are trained for 100 epochs and the weights with the lowest validation loss are saved. We apply class balancing by trimming the dominant class, it has shown to improve the validation results. All models are trained and tested with PyTorch 1.8 on 4 NVIDIA Tesla V100 GPUs and the metrics are calculated with the scikit-learn (v. 1.1.2) package. For 100 epochs, the teacher and student training takes 17 and 16 hours respectively.

To analyze and compare the performance of our method we use the precision (PRE), recall (REC), F1 score (F1) for each class in addition the weighted F1 score ($wF1$)² and total accuracy (ACC) which corresponds to the patients correctly classified. The Cohen’s

²the mean of classes F1 scores weighted by their support

kappa coefficient [44] is calculated with respect to the Gold Standard diagnosis.

4.3 Comparison with state-of-the-art methods and models

We perform a comparison with state-of-the-art methods on WSI classification. For this, we adopt several works:

- HIPT [27] is composed of hierarchical ViTs with self-supervised pretraining on 10,678 WSI from the TCGA open dataset.
- RSP-CR [45] pretrained a ResNet-18 with self-supervision on 69 WSIs. The fine-tuning phase involves consistency regularization.
- CTransPath [47] uses a hybrid CNN-Transformer architecture with self-supervised pretraining on 32,220 WSIs from the TCGA and PAIP datasets. The technique employs semantically relevant contrastive learning for unsupervised pretraining.
- MS-DA-MI [46] introduces a multi-scale domain adversarial training approach for WSI classification using a CNN with MIL.
- DTFD-MIL [18] extends the MIL approach for WSI classification by introducing pseudo-bags with attention-based MIL.
- KimiaNet [22] fine-tuned an ImageNet pretrained DenseNet-121 on 7,126 WSIs from the TCGA dataset with 32 cancer classes.

For training, we use the provided pretrained weights for HIPT, RSP-CR, CTransPath, and the fine-tuned weights for KimiaNet. For the later, we reproduce the same downstream approach in [22] (i.e. we fit a cubic SVM on top of its features). We apply the specific hyperparameters of all methods from their respective paper. The six methods have been trained, validated and tested on our dataset by following the same data split rules adopted for our method. The results are presented in Table 2.

In almost all the measured metrics, our approach shows superior or competitive results when compared to the state-of-the-art methodologies. While CTransPath displays a marginally better ability to correctly identify GCB patients, with a 3% higher recall rate, our model consistently delivers a more balanced performance. Our F-score, a measure that includes both precision (how many selected items are relevant) and recall (how many relevant items are selected), is higher by 2%. This implies that our method is better at both correctly

Table 2: Comparison of the Student model with state-of-the-art methods for WSI classification on test set (64 patients). We estimated the number of floating operations (number of op.) for a WSI diagnosis based on 5 runs.

	ABC			GCB			wF1	ACC \uparrow	number of op. ($\times 10^{12}$)	params.
	PRE	REC	F1	PREC	REC	F1				
HIPT* [27]	0.52	1.00	0.68	0.00	0.00	0.00	0.35	0.52	–	25M
RSP+CR* [45]	0.54	0.94	0.69	0.71	0.16	0.26	0.48	0.56	30.8	11.8M
MS-DA-MI [46]	0.58	0.76	0.66	0.62	0.42	0.50	0.58	0.59	39	67M
KimiaNet* [22]	0.58	0.85	0.69	0.69	0.35	0.47	0.58	0.61	11.5	7M
CTransPath* [47]	0.71	0.73	0.72	0.70	0.68	0.69	0.70	0.70	25	28M
DTFD-MIL [18]	0.68	0.85	0.76	0.78	0.58	0.67	0.71	0.72	18.6	9M
ours (student)	0.72	0.85	0.78	0.80	0.65	0.71	0.75	0.75	0.5	0.89M

* indicates pretrained models

Table 3: Comparison of the Student model with different clinical diagnosis techniques for DLBCL subtyping on test set (64 patients).

	ABC			GCB			
	PRE	REC	F1	PREC	REC	F1	ACC
pathologist A	0.69	0.67	0.68	0.65	0.65	0.65	0.66
pathologist B	0.57	0.64	0.60	0.54	0.45	0.49	0.55
ours (student)	0.72	0.85	0.78	0.80	0.65	0.71	0.75
IHC (Hans et al. [3])	0.92	0.73	0.81	0.76	0.94	0.84	0.83

identifying positive cases and minimizing the number of false positives, providing a more reliable and accurate overall performance. Despite their pretraining on large datasets, models like CTransPath, HIPT, or KimiaNet are still outperformed by our method in effectively distinguishing between the two subtypes, with respective accuracy gaps of +5%, +23%, and +14%. DTFD-MIL, which shows the best results among all comparison methods, is outperformed by our method by +3%. Furthermore, it requires on average $25\times$ more floating operations and contain $10\times$ more parameters than our student model. We see that most methods tend to falsely classify GCB samples as ABC more often than the opposite, which indicates a difficulty to recognize GCB sequences. Indeed, RSP-CR, MS-DA-MIL and KimiaNet show a GCB recall inferior to 0.5 with a critical value of 0.0 for HIPT (i.e. HIPT failed to classify all GCB patients). KimiaNet and DTFD-MIL display a comparable ABC recall than our method (0.85 each), but have inferior GCB recall (0.35, 0.58 and 0.65 respectively). Additionally, we observe that our model is very light compared to other methods, with less than one million parameters, whereas other models contain between 7 and 67 million parameters.

These models face challenges in accurately distinguishing between DLBCL subtypes due to the specific nature of this task. Indeed, because the task is highly complex due to the presence of visually similar features

among the subtypes, these methods also do not escape this complexity and struggle to effectively capture or adapt to it during their training process. On the other hand, by leveraging different modalities, our teacher model learns features that are better suited to the task at hand. The teacher model then provides a crucial supervision to guide the student model to discover the most relevant features for the given task.

4.4 Comparison with medical diagnosis techniques

In Table 3, we compare the student model trained under our method with the visual analysis of two pathologists and the Hans algorithm (presented in section 1). Our model is able to differentiate between the two subtypes more accurately than the two pathologists on HES images, with an accuracy difference of at least 9%. When looking at accuracy, we can see that our model’s performance is closer to the Hans algorithm than to the pathologists’ assessments. It’s important to mention that only the Hans algorithm does better than our model, but only by a small difference of 8%. However, when looking at false negative rates of the two classes in Table 4, our model exhibits a lower rate of ABC patients misclassification than all diagnosis techniques. This means that a patient with ABC subtype (subtype with the lowest survival chances) is less likely to be

misclassified by our model than the Hans algorithm. This assertion is further supported by the ABC class recall rates of 85% for our model and 73% for the Hans algorithm, respectively. As demonstrated by the kappa score, our method (0.5) surpasses the pathologists (0.10 and 0.32) and is closer to the performance of the Hans algorithm (0.66).

We extended our analysis further by visualizing the attention scores of the ViT encoder in the last layer (just before the classification head). To this end, we extracted small regions of test patients HES WSI, and patch the region into sequences of 32×32 patches that we fed to our student model. When looking at the attention scores in Fig. 5, we see tumoral cell rich areas to be the most attended ones. Moreover, areas with high attention score have almost no non-tumoral cells or very few compared to low attention score areas.

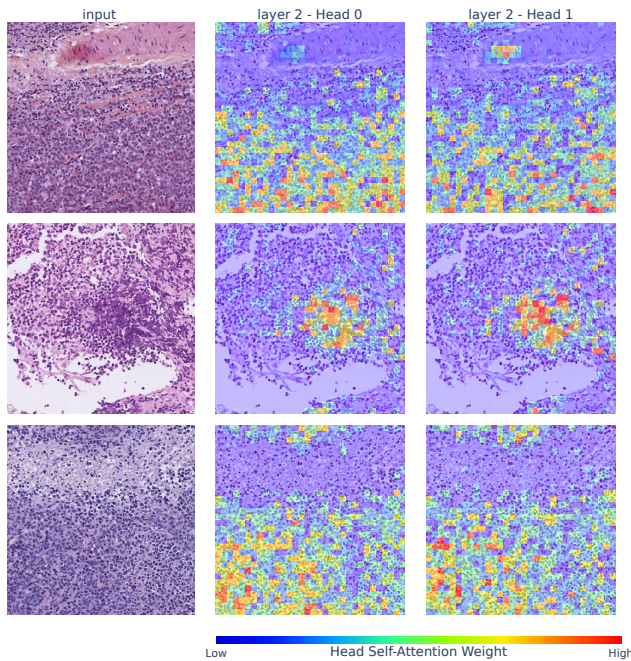


Figure 5: Attention maps of the ViT encoder last layer heads. Each map shows the self-attention scores associated to the class token.

Table 4: False Negative Rates and kappa score (κ) with Gold Standard on test set (64 patients).

	false negative rate		
	ABC	GCB	κ
pathologist A	0.33	0.35	0.32
pathologist B	0.36	0.55	0.10
ours (student)	0.15	0.35	0.50
IHC (Hans et al. [3])	0.27	0.06	0.66

4.5 Power-law scaling

Scaling law in deep learning refers to the model generalization capability when its computational power and/or training data is scaled [48]. It indicates that increasing resources such as the computing power or volume of training data, can considerably improve the model’s efficiency. Studies on ViT [49, 50] have shown that when we increase both the model size and the amount of training data, the generalization error decreases inevitably. In our study, we are interested in observing the student generalization performance when training data is scaled up. We achieved this by training the teacher and student models on varying portions of the original training set, ranging from 10% to 100% of the original size, measured by the number of patients. These subsets are cumulative, meaning each new subset contains all patients from the previous one, with an added 5% patients of the original training set. Thus, with every step, the subset grows by retaining the existing patients and incorporating new ones. Across all subsets, we train the models with the same initial parameters as well as the same hyperparameters, ensuring equal conditions for every trained models. Observing Fig. 6, it is evident that the model accuracy exhibits a general increase with the enlargement of the training data. However, distinct declines in accuracy are observed at 90% and 95%, which could be attributed to the incorporation of patient with images markedly different from the existing dataset. Despite this, the introduction of more patients afterwards leads to a rebound in accuracy, highlighting the positive impact on the model’s performance. For instance, the power-law curve shows that the student model could outperform the Hans algorithm and reach an accuracy of 90% with a training set of 327 patients.

4.6 Ablation study

In this section, we carried out a series of experimental tests to identify the significance of various features incorporated in our architectural design, with the detailed findings listed in Table 5. Our exploration initiated with a thorough analysis of KD, a critical component for its role in guiding the student model using insights from the teacher model. We set up an experiment to train the student model exclusively with the true target, without teacher guidance, to evaluate the impact of such self-reliant learning on generalization performance. Our investigation uncovered interesting findings: without teacher guidance the overall accuracy decreased by 5%. This confirms the essential role of KD pivotal role in improving the student model’s performance and the im-

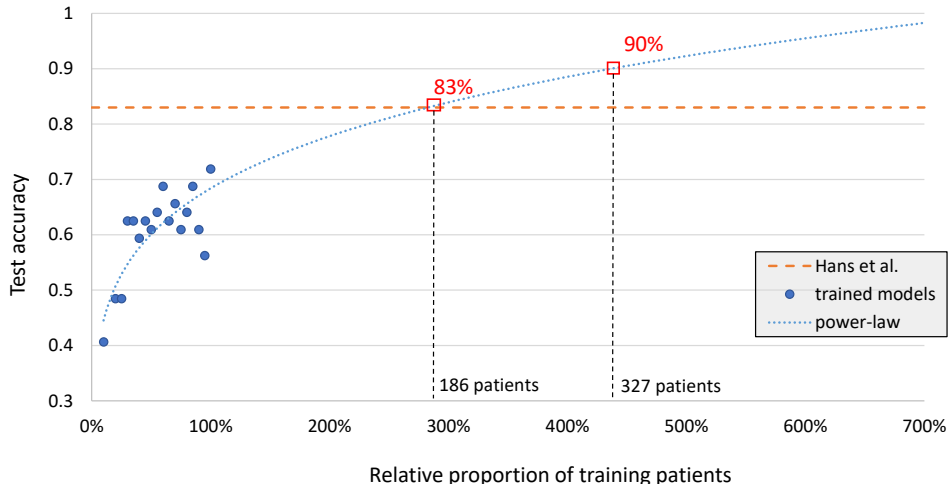


Figure 6: We fit a power-law curve to project the student’s generalization performance in larger training data regimes.

portance of the teacher-student dynamic in the learning process. These insights motivate further research into optimizing KD within our architecture to potentially improve the student model’s performance further.

To minimize the impact of initial parameters choices on the results, we maintained consistent initial model parameters throughout the following experiments. By using the same initial parameters, we could fairly assess the effects of the specific features investigated.

In another experimental setup (*without learnable att.*), substituting learnable attention with dot-product attention led to a notable 17% decrease in accuracy. This resulted in an overall accuracy score even lower than that achieved without any KD at all (58% vs. 70%, respectively). This discrepancy is likely to be attributed to the variations in color distribution between IHC and HES images. These variations may impede the dot-product similarity from effectively capturing relevant information. Therefore, our findings emphasize the crucial role of learnable attention in our methodology. It allows the model to learn to focus on the most relevant IHC information, which is essential for improving the performance of the model.

Next, we removed the softmax activation of the encoder MLP to evaluate its effect on the model’s generalization accuracy (*without softmax*). The modified model demonstrated a substantial decrease in accuracy by 17%, underscoring the essential role of the softmax activation in improving classification performance.

Similarly, we examined the influence of class balancing on the model’s accuracy (*without class balance*). We trained both the teacher and student models without

class balancing. The student model’s accuracy showed a significant decrease of 13%. This suggests that class balancing plays a vital role in the model learning process by ensuring that all classes are equally represented during training.

Table 5: Ablation results on test set (64 patients). We show the F1-score of each class and the total accuracy.

	F1		ACC
	ABC	GCB	
Original (student) model	0.78	0.71	0.75
without softmax	0.54	0.61	0.58
without class balance	0.62	0.57	0.59
without learnable att.	0.61	0.64	0.63
without KD	0.73	0.67	0.70

5 Conclusion

We proposed a new methodology based on knowledge distillation to distill a multi-modal vision transformer-based classifier into a mono-modal one for DLBCL molecular subtyping on WSI. We demonstrated the effectiveness of our methodology through an experimental study on 157 patients. Our mono-modal model outperformed state-of-the-art methods, demonstrating the benefit of leveraging multi-modal model knowledge during training. Additionally, inspired by power-law scaling studies on Vision Transformers, we proposed to study our mono-modal model diagnosis accuracy scaling in

larger training data settings. We found that our model could compete with standard clinical method such as IHC [3] with a reasonable number of additional patients. Because of the difficulty of DLBCL subtyping on HES slides, for a same patient, pathologists often rely on several slides to make a diagnosis. Thus, our methodology could be extended to incorporate these HES slides in the student model training to increase the training data. Moreover, active learning driven data selection has shown to improve generalization of deep learning models while limiting the quantity of data to collect. It could be leveraged to acquire more data efficiently in the objective to reach competitive performance with the Hans algorithm.

Data

The material for conducting the experiments of this work was declared to the French *Commission National de l'Informatique et des Libertés* and the patients were anonymized.

References

- [1] S. H. Swerdlow, "Who classification of tumours of haematopoietic and lymphoid tissues," 2017.
- [2] V. Bobée, P. Ruminy, V. Marchand, P.-J. Vially, A. A. Sater, L. Veresezan, F. Drieux, C. Bérard, É. Bohers, S. Mareschal, S. Dubois, J. P. Jais, K. Leroy, M. Figeac, J. M. Picquenot, T. J. Molina, G. A. Salles, C. Haioun, H. Tilly, and F. Jardin, "Determination of molecular subtypes of diffuse large b-cell lymphoma using a reverse transcriptase multiplex ligation-dependent probe amplification classifier: A calym study.," *The Journal of molecular diagnostics : JMD*, vol. 19 6, pp. 892–904, 2017.
- [3] C. P. Hans, D. D. Weisenburger, T. C. Greiner, R. D. Gascoyne, J. Delabie, G. Ott, H. K. Muller-Hermelink, E. Campo, R. M. Braziel, E. S. Jaffe, Z. Pan, P. Farinha, L. M. Smith, B. Falini, A. H. Banham, A. Rosenwald, L. M. Staudt, J. M. Connors, J. O. Armitage, and W. C. Chan, "Confirmation of the molecular classification of diffuse large b-cell lymphoma by immunohistochemistry using a tissue microarray.," *Blood*, vol. 103 1, pp. 275–82, 2004.
- [4] H. Sung, J. Ferlay, R. L. Siegel, M. Laversanne, I. Soerjomataram, A. Jemal, and F. Bray, "Global cancer statistics 2020: Globocan estimates of incidence and mortality worldwide for 36 cancers in 185 countries," *CA: A Cancer Journal for Clinicians*, vol. 71, pp. 209 – 249, 2021.
- [5] G. Kanas, W. Ge, R. G. W. Quek, K. Keeven, K. Nersesyan, and J. Arnason, "Epidemiology of diffuse large b-cell lymphoma (dlbcl) and follicular lymphoma (fl) in the united states and western europe: population-level projections for 2020–2025.," *Leukemia & Lymphoma*, vol. 63, pp. 54 – 63, 2021.
- [6] A. A. Alizadeh, M. B. Eisen, R. E. Davis, C. Ma, I. S. Lossos, A. Rosenwald, J. C. Boldrick, H. Sabet, T. L. N. Tran, X. Yu, J. I. Powell, L. Yang, G. Marti, T. Moore, J. I. Hudson, L.-S. Lu, D. B. Lewis, R. Tibshirani, G. Sherlock, W. C. Chan, T. C. Greiner, D. D. Weisenburger, J. O. Armitage, R. A. Warnke, R. Levy, W. H. Wilson, M. R. Graver, J. C. Byrd, D. Botstein, P. Brown, and L. M. Staudt, "Distinct types of diffuse large b-cell lymphoma identified by gene expression profiling," *Nature*, vol. 403, pp. 503–511, 2000.
- [7] S. Mareschal, P. Ruminy, C. Bagacean, V. Marchand, M. Cornic, J. P. Jais, M. Figeac, J. M. Picquenot, T. J. Molina, T. Fest, G. A. Salles, C. Haioun, K. Leroy, H. Tilly, and F. Jardin, "Accurate classification of germinal center b-cell-like/activated b-cell-like diffuse large b-cell lymphoma using a simple and rapid reverse transcriptase-multiplex ligation-dependent probe amplification assay: A calym study.," *The Journal of molecular diagnostics : JMD*, 2015.
- [8] A. Rosenwald and L. M. Staudt, "Gene expression profiling of diffuse large b-cell lymphoma.," *Leukemia & Lymphoma*, vol. 44, pp. S41 – S47, 2003.
- [9] G. E. Wright, B. K. Tan, A. Rosenwald, E. H. Hurt, A. Wiestner, and L. M. Staudt, "A gene expression-based method to diagnose clinically distinct subgroups of diffuse large b cell lymphoma.," *Proceedings of the National Academy of Sciences of the United States of America*, vol. 100, pp. 9991 – 9996, 2003.
- [10] G. S. Nowakowski, B. R. Laplant, W. R. Macon, C. B. Reeder, J. M. Foran, G. D. Nelson, C. A. Thompson, C. E. Rivera, D. J. Inwards, I. N. Micallef, P. B. Johnston, L. F. Porrata, S. M. Ansell, R. D. Gascoyne, T. M. Habermann, and T. E. Witzig, "Lenalidomide combined with r-chop overcomes negative prognostic impact of non-germinal center b-cell phenotype in newly diagnosed diffuse large b-cell lymphoma: a phase ii study.," *Journal of clinical oncology : official journal of the*

American Society of Clinical Oncology, vol. 33 3, pp. 251–7, 2015.

- [11] G. S. Nowakowski, A. Chiappella, R. D. Gascoyne, D. W. Scott, Q. Zhang, W. Jurczak, M. Özcan, X. nan Hong, J. Zhu, J. Jin, D. Belada, J. M. Bergua, F. Piazza, H. Mociková, A. L. Molinari, D. H. Yoon, F. Cavallo, M. Tani, K. Yamamoto, K. Izutsu, K. Kato, M. S. Czuczman, S. Hersey, A. Kilcoyne, J. Russo, K. Hudak, J. Zhang, S. Wade, T. E. Witzig, and U. Vitolo, “Robust: A phase iii study of lenalidomide plus r-chop versus placebo plus r-chop in previously untreated patients with abc-type diffuse large b-cell lymphoma,” *Journal of Clinical Oncology*, vol. 39, pp. 1317 – 1328, 2021.
- [12] P. K. Mishro, S. Agrawal, R. Panda, and A. Abraham, “A survey on state-of-the-art denoising techniques for brain magnetic resonance images.,” *IEEE reviews in biomedical engineering*, vol. PP, 2021.
- [13] F. Xing, Y. Xie, H. Su, F. Liu, and L. Yang, “Deep learning in microscopy image analysis: A survey,” *IEEE Transactions on Neural Networks and Learning Systems*, vol. 29, pp. 4550–4568, 2018.
- [14] M. Z. Atwany, A. Sahyoun, and M. Yaqub, “Deep learning techniques for diabetic retinopathy classification: A survey,” *IEEE Access*, vol. PP, pp. 1–1, 2022.
- [15] C. L. Srinidhi, O. Ciga, and A. L. Martel, “Deep neural network models for computational histopathology: A survey,” *Medical image analysis*, vol. 67, p. 101813, 2019.
- [16] M. Y. Lu, D. F. K. Williamson, T. Y. Chen, R. J. Chen, M. Barbieri, and F. Mahmood, “Data-efficient and weakly supervised computational pathology on whole-slide images,” *Nature Biomedical Engineering*, vol. 5, pp. 555 – 570, 2020.
- [17] X. Wang, H. Chen, C. Gan, H. Lin, Q. Dou, E. Tsougenis, Q. Huang, M. Cai, and P.-A. Heng, “Weakly supervised deep learning for whole slide lung cancer image analysis,” *IEEE Transactions on Cybernetics*, vol. 50, pp. 3950–3962, 2020.
- [18] H. Zhang, Y. Meng, Y. Zhao, Y. Qiao, X. Yang, S. E. Coupland, and Y. Zheng, “Dtf-d-mil: Double-tier feature distillation multiple instance learning for histopathology whole slide image classification,” *2022 IEEE/CVF Conference on Computer Vision and Pattern Recognition (CVPR)*, pp. 18780–18790, 2022.
- [19] S. Graham, Q. D. Vu, S. E. A. Raza, A. Azam, Y.-W. Tsang, J. T. Kwak, and N. M. Rajpoot, “Hovernet: Simultaneous segmentation and classification of nuclei in multi-tissue histology images,” *Medical image analysis*, vol. 58, p. 101563, 2018.
- [20] N. Hashimoto, Y. Takagi, H. Masuda, H. Miyoshi, K. Kohno, M. Nagaishi, K. Sato, M. Takeuchi, T. Furuta, K. Kawamoto, K. Yamada, M. Moritsubo, K. Inoue, Y. Shimasaki, Y. Ogura, T. Imamoto, T. Mishina, K. Ohshima, H. Hontani, and I. Takeuchi, “Case-based similar image retrieval for weakly annotated large histopathological images of malignant lymphoma using deep metric learning,” *Medical image analysis*, vol. 85, p. 102752, 2021.
- [21] N. Hegde, J. D. Hipp, Y. Liu, M. R. Emmert-Buck, E. Reif, D. Smilkov, M. Terry, C. J. Cai, M. B. Amin, C. H. Mermel, P. Q. Nelson, L. H. Peng, G. S. Corrado, and M. C. Stumpe, “Similar image search for histopathology: Smily,” *NPJ Digital Medicine*, vol. 2, 2019.
- [22] A. Riasatian, M. Babaie, D. Maleki, S. Kalra, M. Valipour, S. Hemati, M. Zaveri, A. Safarpour, S. Shafiei, M. Afshari, M. Rasoolijaberi, M. Sikaroudi, M. Adnan, S. Shah, C. Choi, S. Damaskinos, C. J. V. Campbell, P. Diamandis, L. X. Pantanowitz, H. Kashani, A. Ghodsi, and H. R. Tizhoosh, “Fine-tuning and training of densenet for histopathology image representation using tcga diagnostic slides,” *Medical image analysis*, vol. 70, p. 102032, 2021.
- [23] D. Guidolin, R. Tamma, T. Annese, C. Tortorella, G. Ingravallo, F. Gaudio, T. Perrone, P. Musto, G. Specchia, and D. Ribatti, “Different spatial distribution of inflammatory cells in the tumor microenvironment of abc and gbc subgroups of diffuse large b cell lymphoma,” *Clinical and Experimental Medicine*, vol. 21, pp. 573 – 578, 2021.
- [24] S. Deng, X. Zhang, W. Yan, E. I.-C. Chang, Y. Fan, M. Lai, and Y. Xu, “Deep learning in digital pathology image analysis: a survey,” *Frontiers of Medicine*, vol. 14, pp. 470 – 487, 2020.
- [25] G. Campanella, M. G. Hanna, L. Geneslaw, A. P. Mirafior, V. W. K. Silva, K. J. Busam, E. Brogi, V. E. Reuter, D. S. Klimstra, and T. J. Fuchs, “Clinical-grade computational pathology using weakly supervised deep learning on whole slide images,” *Nature Medicine*, pp. 1–9, 2019.

- [26] R. J. Chen and R. G. Krishnan, "Self-supervised vision transformers learn visual concepts in histopathology," *ArXiv*, vol. abs/2203.00585, 2022.
- [27] R. J. Chen, C. Chen, Y. Li, T. Y. Chen, A. D. Trister, R. G. Krishnan, and F. Mahmood, "Scaling vision transformers to gigapixel images via hierarchical self-supervised learning," *2022 IEEE/CVF Conference on Computer Vision and Pattern Recognition (CVPR)*, pp. 16123–16134, 2022.
- [28] Z. Shao, H. Bian, Y. Chen, Y. Wang, J. Zhang, X. Ji, and Y. Zhang, "Transmil: Transformer based correlated multiple instance learning for whole slide image classification," in *Neural Information Processing Systems*, 2021.
- [29] H. E. Achi, T. Belousova, L. Chen, A. Wahed, I. Wang, Z. J. Hu, Z. Kanaan, A. Rios, and A. N. D. Nguyen, "Automated diagnosis of lymphoma with digital pathology images using deep learning," *Annals of clinical and laboratory science*, vol. 49 2, pp. 153–160, 2018.
- [30] H. Miyoshi, K. Sato, Y. Kabeya, S. Yonezawa, H. Nakano, Y. Takeuchi, I. Ozawa, S. Higo, E. Yanagida, K. Yamada, K. Kohno, T. Furuta, H. Muta, M. Takeuchi, Y. Sasaki, T. Yoshimura, K. Matsuda, R. Muto, M. Moritsubo, K. Inoue, T. Suzuki, H. Sekinaga, and K. Ohshima, "Deep learning shows the capability of high-level computer-aided diagnosis in malignant lymphoma," *Laboratory Investigation*, pp. 1–11, 2020.
- [31] G. Steinbuss, M. Kriegsmann, C. Zgorzelski, A. Brobeil, B. Goepfert, S. Dietrich, G. Mechttersheimer, and K. Kriegsmann, "Deep learning for the classification of non-hodgkin lymphoma on histopathological images," *Cancers*, vol. 13, 2021.
- [32] F. Gaudio, R. Tamma, G. Ingravallo, T. Perrone, F. E. Laddaga, M. S. D. Candia, E. Maiorano, D. Ribatti, and G. Specchia, "Computer-driven quantitative image analysis in the assessment of tumor cell and t cell features in diffuse large b cell lymphomas," *Annals of Hematology*, vol. 97, pp. 663–668, 2018.
- [33] N. Hashimoto, K. Ko, T. Yokota, K. Kohno, M. Nakaguro, S. Nakamura, I. Takeuchi, and H. Hontani, "Subtype classification of malignant lymphoma using immunohistochemical staining pattern," *International Journal of Computer Assisted Radiology and Surgery*, vol. 17, pp. 1379 – 1389, 2022.
- [34] D. Li, J. R. Bledsoe, Y. Zeng, W. Liu, Y. Hu, K. Bi, A. Liang, and S. Li, "A deep learning diagnostic platform for diffuse large b-cell lymphoma with high accuracy across multiple hospitals," *Nature Communications*, vol. 11, 2020.
- [35] R. Nakhli, P. A. Moghadam, H. Mi, H. S. Farahani, A. S. Baras, C. B. Gilks, and A. Bashashati, "Amigo: Sparse multi-modal graph transformer with shared-context processing for representation learning of giga-pixel images," *ArXiv*, vol. abs/2303.00865, 2023.
- [36] B. Korbar, A. M. Olofson, A. P. Mirafior, K. M. Nicka, M. A. Suriawinata, L. Torresani, A. A. Suriawinata, and S. Hassanpour, "Deep learning for classification of colorectal polyps on whole-slide images," *Journal of Pathology Informatics*, vol. 8, 2017.
- [37] M. Kim, H. Sekiya, G. Yao, N. B. Martin, M. Castanedes-Casey, D. W. Dickson, T. H. Hwang, and S. Koga, "Diagnosis of alzheimer's disease and tauopathies on whole slide histopathology images using a weakly supervised deep learning algorithm," *Laboratory investigation; a journal of technical methods and pathology*, p. 100127, 2023.
- [38] Y. Dong, Z. Jiang, H. Shen, W. D. Pan, L. A. Williams, V. V. B. Reddy, W. H. Benjamin, and A. W. Bryan, "Evaluations of deep convolutional neural networks for automatic identification of malaria infected cells," *2017 IEEE EMBS International Conference on Biomedical & Health Informatics (BHI)*, pp. 101–104, 2017.
- [39] C. Dwivedi, S. Nofallah, M. Pouryahya, J. Iyer, K. Leidal, C. Chung, T. Watkins, A. N. Billin, R. Myers, J. Abel, and A. Behrooz, "Multi stain graph fusion for multimodal integration in pathology," *2022 IEEE/CVF Conference on Computer Vision and Pattern Recognition Workshops (CVPRW)*, pp. 1834–1844, 2022.
- [40] M. Hu, M. Maillard, Y. Zhang, T. Ciceri, G. L. Barbera, I. Bloch, and P. Gori, "Knowledge distillation from multi-modal to mono-modal segmentation networks," in *International Conference on Medical Image Computing and Computer-Assisted Intervention*, 2020.
- [41] A. Dosovitskiy, L. Beyer, A. Kolesnikov, D. Weissenborn, X. Zhai, T. Unterthiner, M. Dehghani, M. Minderer, G. Heigold, S. Gelly, J. Uszkoreit, and N. Houlsby, "An image is worth 16x16

- words: Transformers for image recognition at scale,” *ArXiv*, vol. abs/2010.11929, 2020.
- [42] J. Ba, J. R. Kiros, and G. E. Hinton, “Layer normalization,” *ArXiv*, vol. abs/1607.06450, 2016.
- [43] R. Müller, S. Kornblith, and G. E. Hinton, “When does label smoothing help?,” in *Neural Information Processing Systems*, 2019.
- [44] M. L. McHugh, “Interrater reliability: the kappa statistic,” *Biochemia Medica*, vol. 22, pp. 276 – 282, 2012.
- [45] C. L. Srinidhi, S. W. Kim, F.-D. Chen, and A. L. Martel, “Self-supervised driven consistency training for annotation efficient histopathology image analysis,” *Medical image analysis*, vol. 75, p. 102256, 2021.
- [46] N. Hashimoto, D. Fukushima, R. Koga, Y. Takagi, K. Ko, K. Kohno, M. Nakaguro, S. Nakamura, H. Hontani, and I. Takeuchi, “Multi-scale domain-adversarial multiple-instance cnn for cancer subtype classification with unannotated histopathological images,” *2020 IEEE/CVF Conference on Computer Vision and Pattern Recognition (CVPR)*, pp. 3851–3860, 2020.
- [47] X. Wang, S. Yang, J. Zhang, M. Wang, J. Zhang, W. Yang, J. Huang, and X. Han, “Transformer-based unsupervised contrastive learning for histopathological image classification,” *Medical image analysis*, vol. 81, p. 102559, 2022.
- [48] J. Hestness, S. Narang, N. Ardalani, G. F. Diamos, H. Jun, H. Kianinejad, M. M. A. Patwary, Y. Yang, and Y. Zhou, “Deep learning scaling is predictable, empirically,” *ArXiv*, vol. abs/1712.00409, 2017.
- [49] X. Zhai, A. Kolesnikov, N. Houlsby, and L. Beyer, “Scaling vision transformers,” *2022 IEEE/CVF Conference on Computer Vision and Pattern Recognition (CVPR)*, pp. 1204–1213, 2021.
- [50] S. Abnar, M. Dehghani, B. Neyshabur, and H. Sedghi, “Exploring the limits of large scale pre-training,” *ArXiv*, vol. abs/2110.02095, 2021.